Received: 7 July 2020 | Revised: 26 October 2020 | Accepted: 12 November 2020

DOI: 10.1002/pip.3380

EU PVSEC PAPER

WILEY PROGRESS IN PHOTOVOLTAICS

Electronic and compositional properties of the rear-side of stoichiometric $CuInSe_2$ absorbers

Christian Kameni Boumenou[1] | Amala Elizabeth[2,3] | Finn Babbe[1,4] | Alice Debot[1] | Harry Mönig[2,3] | Alex Redinger[1]

[1]Department of Physics and Materials Science, University of Luxembourg, Luxembourg City, L-1511, Luxembourg

[2]Physikalisches Institut, Westfälische Wilhelms-Universität Münster, Münster, Germany

[3]Center for Nanotechnology (CeNTech), Münster, Germany

[4]Chemical Sciences Division, Lawrence Berkeley National Laboratory, Berkeley, California, 94720, USA

Correspondence
Alex Redinger, Department of Physics and Materials Science, University of Luxembourg, Luxembourg City L-1511, Luxembourg.
Email: alex.redinger@uni.lu

Funding information
Deutsche Forschungsgemeinschaft, Grant/Award Number: MO 2345/5-1 ;Fonds National de la Recherche Luxembourg (FNR), Grant/Award Number: 11244141

Abstract

In-depth understanding and subsequent optimization of the contact layers in thin film solar cells are of high importance in order to reduce the amount of nonradiative recombination and thereby improve device performance. In this work, the buried $MoSe_2/CuInSe_2$ interface of stoichiometric absorbers is investigated with scanning tunneling spectroscopy and Kelvin probe force microscopy combined with compositional measurements acquired via photo-electron spectroscopy after a mechanical lift-off process. We find that the local density of states, as measured with scanning tunneling spectroscopy, is similar to the front-side of ultra-high vacuum annealed CISe absorbers. The grain boundaries exhibit a weak upward band bending, opposite to Cu-poor $CuGaSe_2$, and we measure an increased Cu accumulation at the rear CISe surface compared to the bulk composition and a non-zero concentration of Cu on the Mo-side. Grazing incidence X-ray diffraction measurements corroborate that a small amount of a Cu_xSe secondary phase is present at the $MoSe_2/CuInSe_2$ interface in contrast to reports on Cu-poor material. Our findings shed new light into the complex interface formation of $CuInSe_2$-based thin film solar cells grown under Cu-rich conditions.

KEYWORDS
$CuInSe_2$, Kelvin probe force microscopy, scanning tunneling microscopy

1 | INTRODUCTION

$Cu(In,Ga)Se_2$ (CIGSe) thin film solar cells offer high power conversion efficiencies (PCE),[1] low energy payback time, and long-term stability.[2] Several major breakthroughs in the last decades allowed this material system to surpass the 20% efficiency benchmark on rigid and flexible substrates[1,3] and PCEs as high as 23.35% were reported.[1] One of the important steps that allowed for high PCE was the introduction of a Gallium back-gradient, which effectively reduced the recombination at the $Mo/MoSe_2$ back-contact.[4,5] The optimization of this interface is still an area of intensive research due to the following reasons: The Molybdenum back-contact interface has a poor optical reflectivity and the recombination velocity is high,[6] which means that effective passivation strategies are indispensable. This is especially true for ultra-thin devices[7] where bandgap grading is not feasible.

Pure $CuInSe_2$ (CISe) solar cells have several advantages compared to CIGSe such as an easier manufacturing process and a lower bandgap, which makes this material more attractive for tandem applications. However, the PCE was stuck for a long time at 15%[8] without post deposition treatment. Recently, KF treatment improved this number to 16%,[9] which is still far away from the record CIGSe absorbers. It was shown that the likely reason for the lower CISe solar cell performance

[Correction added on 11 January 2021, after first online publication: surname of 'Harry Mönig' has been corrected in this version.]

was the absence of the Ga back-contact grading.[10] The minority carrier lifetime improved after exfoliation of the absorber layer from the back-contact, which showed that recombination at the back is a major issue in nongraded CISe absorbers. Meanwhile, some laboratories showed that a Ga back-grading could be introduced in CIGSe in a way that the bandgap was still close to the pure CISe, which resolves the disadvantage for tandem applications,[11,12] albeit increasing the complexity of the process. In agreement with the previous discussion, the PCE increased, and meanwhile, above 19-% efficient solar cells were reported with a bandgap close to 1.0 eV.[12]

There are already quite a few important reports that focused on the buried $MoSe_2$/CI(G)S(e) interface, which mostly relied on the fact that the absorber could be peeled off mechanically from the back-contact.[10,13,14] This made it possible to use surface sensitive techniques such as X-ray and UV photo-electron spectroscopy (XPS/UPS) to study compositional and electronic variations at that interface. It was shown that there is a Ga accumulation at the back-contact[15] and the $CuInS_2$ (CIS) back-surface was Cu-depleted despite Cu-rich growth conditions.[13] Transmission electron microscopy measurements (TEM) showed that there was some in-diffusion of Cu into the Mo[16] and atom probe tomography (APT) measurements showed an increased Cu and Ga concentration in the first 50 nm of the CIGSe absorber (measured from the back-surface).[17] Most of these measurements were performed on Cu-poor CIGSe (Cu/In<1). For the case of $CuGaSe_2$, grown under Cu-excess, it was shown via TEM measurements that Cu_xSe precipitations could also exist in the bulk of the absorber layer.[18] Already at that time, it was speculated that this may be the reason for the low efficiencies of Cu-rich absorber layers. However, until today, the general consensus in the community is that Cu-rich absorbers exhibit a secondary phase free bulk with Cu_xSe on top, which can be etched away via a potassium cyanide etching step.[19]

Much less is known about the lateral variations of the electrical properties on the nanometer scale of the back-surface. A detailed combined electron beam induced current (EBIC) and cathodoluminescence (CL) study[6] showed that, for a number of absorbers with different compositions, the grain boundary properties varied and there was no direct correlation between the CL signal and the collection efficiency, as measured via EBIC. For low symmetry grain boundaries, CL measurements showed a reduced signal, which pointed towards an increased number of defects at the grain boundaries. Furthermore, there are some Kelvin probe force microscopy (KPFM) measurements available[20] on $CuGaSe_2$, which showed that most of the grain boundaries exhibited downward band bending in the order of approximately 50 meV compared to the grain surfaces. Furthermore, Ga remnants were found on the Mo-side. So far, no scanning probe microscopy measurements are available for CISe.

It is well known in the CI(G)Se community that the Cu-content is very important.[21,22] High performance CIGSe devices are grown under Cu-poor conditions (Cu/In<1), which improves V_{OC} and quasi-Fermi level splitting compared to Cu/In>1.[22] For Ga-free CISe absorbers, the difference in quasi-Fermi level splitting between Cu-poor and Cu-rich absorbers is small.[23,24] However, in agreement with the Ga-containing absorbers, the PCE is higher for Cu-poor than for Cu-rich devices. In the case of Cu-rich absorbers, the excess Cu condensates as Cu_xSe on top of the CISe absorbers. A subsequent potassium cyanide (KCN) etching[13,25] removes the Cu_xSe (or Cu_xS in the case of CIS), thereby creating a stoichiometric absorber with less Cu-vacancies in the bulk. The KCN etching, however, also has some adverse effects on the composition and defects in the near surface region.[26,27] The investigation of the rear-surface thereby offers a very nice opportunity to investigate stoichiometric absorbers (grown Cu-rich) without KCN etching.

In this contribution, stoichiometric CISe absorbers (grown Cu-rich and subsequently KCN etched) were mechanically peeled off from their substrate and systematically scrutinized by means of scanning probe microscopy (SPM) techniques such as scanning tunneling microscopy (STM) and Spectroscopy (STS) and KPFM. The local density of states was evaluated by STS and compared to measurements performed at the top surface[27-30] whereas variations in workfunction of the films were probed by KPFM in order to compare the results to already published data on $CuGaSe_2$.[20] Additionally, XPS and energy dispersive X-ray analysis (EDX) were used to explore the surface and bulk compositions and the impact of the peeling process on quasi-Fermi level splitting was investigated with photoluminescence (PL) imaging. Finally, X-ray diffraction measurements were used to investigate the occurrence of secondary phases in the CISe absorber layers.

2 | EXPERIMENTAL DETAILS

SPM measurements were performed in a variable temperature ultra-high vacuum system with a base pressure in the 10^{-11} mbar range. The STM and STS measurements were acquired using chemically etched tungsten tips, cleaned in situ by voltage pulses, on a clean gold substrate, anterior to the measurements of the $CuInSe_2$ films. The local density of states (LDOS) of the absorbers were acquired via current imaging tunneling spectroscopy (CITS) maps at several regions of the absorbers in order get representative data. The analyzed areas range from $1\times1\ \mu m^2$ to $4\times4\ \mu m^2$. For each CITS map, a grid of 120× 120 pixels was defined at which a current-voltage (*I*-*U*) curve was acquired while the feedback loop was switched off. In the present study, the voltage was swept from −2*V* to +2*V*. Thereafter, the LDOS, which is proportional to dI/dU,[31] was derived by numerical differentiation of the current *I* with respect to the applied voltage *U*.

Work function maps were measured using frequency modulation Kelvin probe force microscopy (FM-KPFM), which compensates the electrostatic force gradient between a sharp conductive tip and the sample, providing a credible and accurate contact potential difference (CPD) value, combined with an excellent lateral resolution.[32,33] The measurements were performed with the bias applied to the sample and Pt-Ir coated Si-cantilevers with the following nominal characteristics were used: resonance frequency 75 kHz, tip radius 20 nm, length 215–235 μm, width 20–35 μm, set-point for topography measurements −5 Hz.

The absorbers analyzed in this study were synthesized via coevaporation on molybdenum coated soda lime glass (SLG) substrates at a nominal temperature of 580°C. A detailed description of the growth process can be found in Deprédurand et al.[34] Typical device performances from Cu-rich absorbers are in the range of 8%–10%.

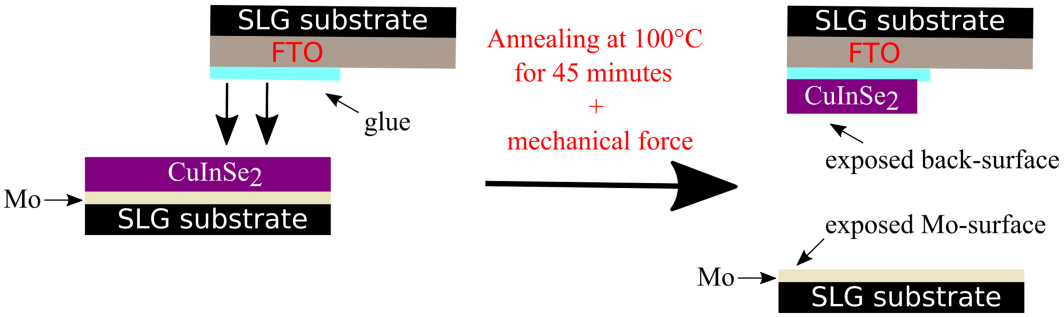

FIGURE 1 Simplified schematic of the exfoliation process of the CISe absorbers. In a first step, a fluorine doped tin-oxide coated glass substrate was glued on top of the CISe absorber. After curing and application of mechanical force, an exfoliation at the $MoSe_2$/CISe interface could be achieved. The exfoliation was done in a N_2-filled glovebox to prevent oxidation. [Colour figure can be viewed at wileyonlinelibrary.com]

In order to examine the back-side of the absorbers, they were peeled off from their original substrates following the procedure schematized in Figure 1. The samples were glued to clean fluorine doped tin oxide coated glass substrates using a ultra-high vacuum (UHV) compatible Ag epoxy glue. Curing was performed in air on a hot plate at ≈100°C for 45 min. Afterwards the samples were transferred into a nitrogen filled glove box ($H_2O < 1$ ppm; $O_2 < 1$ ppm) where they were exfoliated and introduced into the SPM analysis chamber without exposing them to air. This was accomplished by means of a vacuum suitcase. A similar procedure was followed for the XPS analysis. PL and EDX investigations were accomplished on the same absorbers (produced during the same growth process). For these measurements, a short air exposure could not be circumvented. For the PL measurements, the time between cleaving and measuring was of the order of 10 minutes.

For the XPS measurements, the samples were glued in Luxembourg and then shipped to Münster in a N_2-filled transport box. The samples were again introduced into a N_2 filled glovebox, which was connected to the UHV system. The samples were cleaved in this box and directly introduced into the XPS chamber. Thereby, the back-surface was only exposed to N_2 for a few minutes. Because only one sample could be loaded at a time, the Mo-side was kept in N_2 and introduced into UHV the day after. The XPS setup was calibrated on clean single-crystal metal surfaces prior to the measurements of the CISe back-side and of the Mo-side. The base pressure of the XPS system was in the 10^{-11} mbar range and a monochromatic Al K_α X-ray source was used for the XPS measurements.

In order to compare the near-surface composition to the bulk composition, additional EDX measurements were performed on both the front-side and back-side of the films using 20, 15, 7, and 5 kV acceleration voltage. Elemental compositions were deduced via the well-known ZAF method[35] without standardization.

Grazing incidence X-ray diffraction measurements were carried out at an incident angle of 1° in a parallel beam configuration. The measurements were carried on samples, which were first KCN etched in order to remove a Cu_xSe secondary phase at the front surface and subsequently cleaved, as discussed in the previous paragraphs.

The impact of the cleaving and of the Ag epoxy glue on opto-electronic properties was analyzed with PL imaging performed in a custom built system. A 532-nm pulsed laser illuminated an area of approximately 2×2 cm^2. The generated PL signal was collected with an InGaAs camera, with a high quantum efficiency in the range of 800 to 1600 nm. The system was calibrated to absolute photon numbers in order to estimate the PL quantum efficiency and the quasi-Fermi level splitting of the absorber before and after the peeling process.

3 | RESULTS

3.1 | The $MoSe_2$/CISe interface

Figure 2A shows a representative STM image of the rear-surface of a Cu-rich $CuInSe_2$ absorber layer. The surface is very flat with an RMS roughness of 8 nm. The locations of the grain boundaries are well visible in the image as they exhibit a slightly lower height than the grain interior. The large grains are covered with tiny little grains, which we observed in all of the images we analyzed. Furthermore, some deep holes (black contrast) were observed, which were likely to be caused by pinholes in the absorber layer prior or during the peeling process. In Figure 2B, the corresponding STM image of the Mo-side is presented, where no indications of grain boundaries were found. The surface was covered with small precipitates, which had an extension of approximately 70 nm.

In order to corroborate that the absorber peeled at the $MoSe_2$/CISe interface, XPS measurements were carried out on both samples (back-side and Mo-side) and the scans are presented in Figure 2C. On the back-side, we did observe all the peaks of the CISe matrix, that is, Cu, In, and Se. Contrary, the Mo-side did only show peaks that are related to Mo and Se in the survey scan. At a later stage of the manuscript, we will discuss high resolution scans in more detail. In contrast to the survey scan presented in Figure 2C, we found a very small amount of Cu on the Mo side but no traces of In. The XPS measurements corroborated that the absorber cleaved exactly at the $MoSe_2$/CISe interface in accordance with previous reports[6,13,20] due to the formation of a $MoSe_2$ layer during synthesis, which is known to be a van der Waals solid where exfoliation is feasible.

The higher oxygen signal at the Mo-side was likely to be caused by the longer storage time of this sample compared to the back-side as discussed in the experimental part.

We also found an Ag peak in the XPS spectra, which we related to glue that was present at the edges of the exfoliated absorber due to the small size of these samples (see Figure 2F). Complementary EDX measurements showed that the Ag concentration in the bulk is lower than 1 at%, which is within the experimental error of the machine, considering the close distance of the In and Ag L-lines

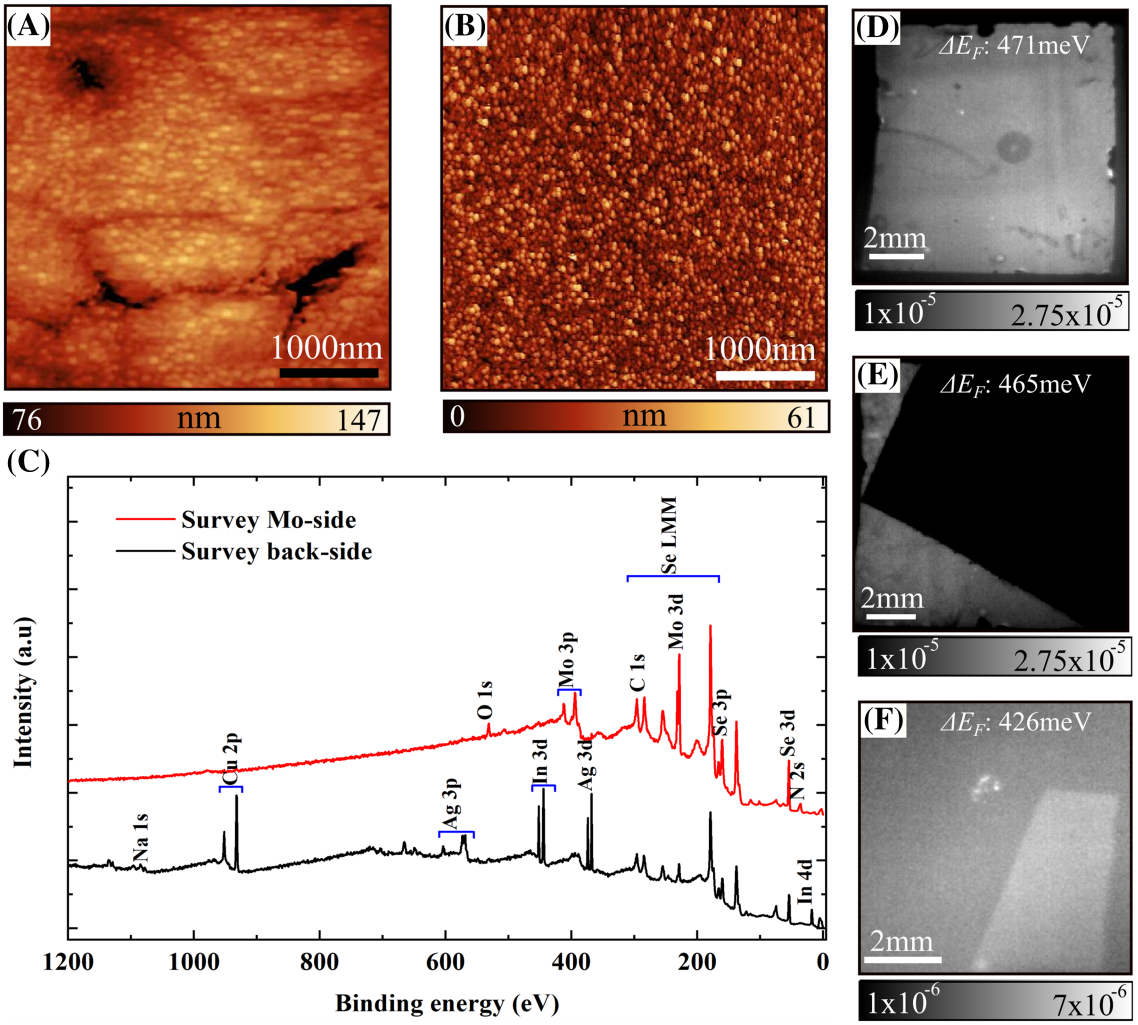

FIGURE 2 (A) STM image of the back-surface of the CISe absorber. (B) STM image of the exposed $MoSe_2$ surface after cleaving. Scan parameters: I= 1nA, U= −2V, (C) XPS survey scan. Important to note is the absence of the Cu and In peaks on the Mo-side and the absence of Mo on the backside. High resolution scans will be discussed at a later stage of this report. (D) PL mapping of the absorber top-surface before cleaving and gluing (E) top-surface of the CISe absorber after exfoliation. The dark region is where the CISe absorber was removed from the substrate. (F) PL image of the exfoliated part. The PL image was performed via illumination from the rear-surface. (D–F) The PL yield indicated on the scale bar is given in PL quantum yield, which was converted to a quasi-Fermi level splitting ΔE_F via Equation (1) [Colour figure can be viewed at wileyonlinelibrary.com]

(In_L: 3.286 keV vs Ag_L: 2.984 keV). In order to check if the absorber layer was still intact after the peeling process, we carried out PL imaging measurements before the gluing and after the peeling process and the results are presented in Figure 2D–F. The scale bar is given in units of PL quantum yield (PLQY), which is defined as the quotient of the PL yield (photons/$cm^2 \cdot s$) emitted from the sample Y_{out} to the impinging photon density Y_{in} generated by the laser. This quantity can then be used to extract the quasi Fermi-level splitting ΔE_F of the absorbers via Equation (1).[36]

$$\Delta E_F = \Delta E_F^{rad} + k_B T \ln\left[\frac{Y_{out}}{Y_{in}}\right]. \quad (1)$$

ΔE_F^{rad} refers to the maximum achievable V_{OC} in the absence of non-radiative recombination. In our case, the bandgap of the absorber is 1.0 eV, which translated to ΔE_F^{rad}=749 meV.[37,38] The remaining constants in Equation (1) are the temperature T at which the sample was measured and the Boltzmann constant k_B. From the measurement right after KCN etching, we deduced a ΔE_F=471 meV (measured by illuminating the front side of the CISe), which is a typical value for Cu-rich $CuInSe_2$ absorbers.[23,24] After the gluing process and the subsequent liftoff, the non-cleaved part of the absorber did not change significantly and ΔE_F = 465 meV was very close to the fresh case (still measuring the front-side of the CISe absorber). The result of the back-surface, which is presented in Figure 2F shows a somewhat reduced ΔE_F of only 426 meV. This showed that the gluing and exfoliation procedure had a negative impact on the opto-electronic properties of the absorber layer. However, it is important to note here that the absorber was still intact and ΔE_F = 426 meV was only 39 meV lower, which ruled out extensive metallic in-diffusion of Ag that would have increased nonradiative recombination massively. We also note that the roughness of the exposed back-contact was extremely low, in contrast to the front-surface, which may also have altered the reflection coefficient of the impinging laser light and thereby the reabsorption probability of the emitted photons, which also has an impact on PLQY.[39] From this analysis, we concluded that the peeling process of the back-surface was successful and that this procedure did

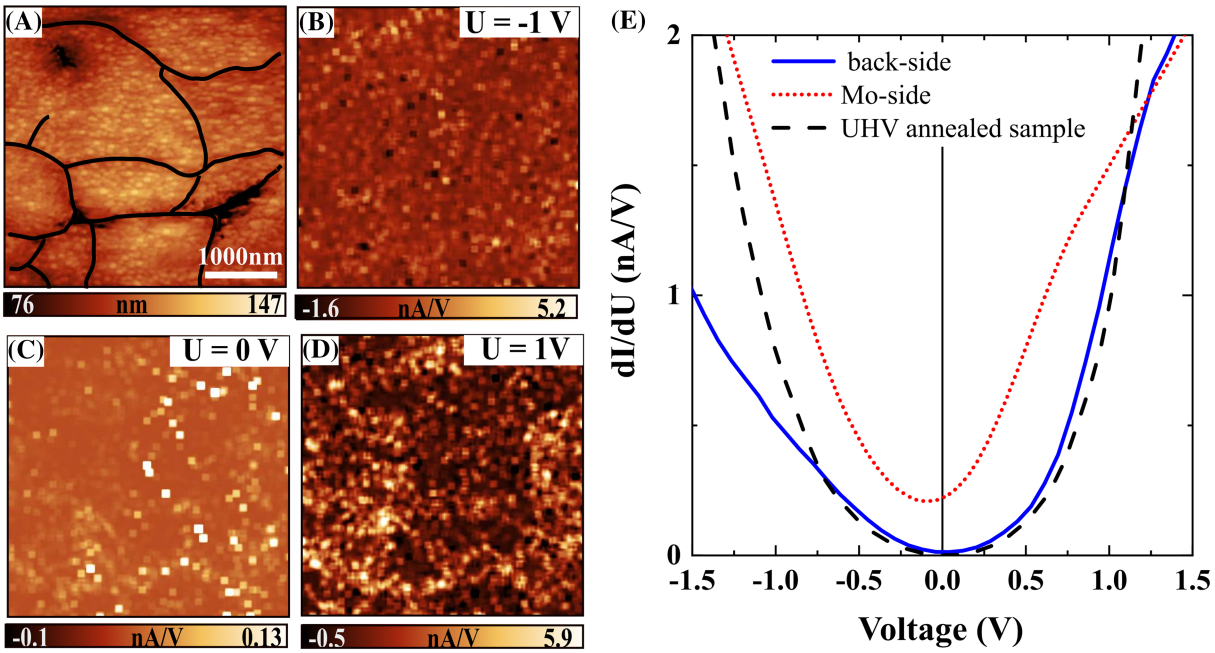

FIGURE 3 (A) STM topography image of the back-surface of the CISe absorber layer. The black lines highlight the position of the grain boundaries. (B–D) *dI*/*dU*-CITS maps at different applied voltages of the region shown in Figure 2A. The measurements were performed at a tunneling set-point of 1 nA and the voltage was changed from −2 V to +2V. The blue solid, red dotted, and black dashed curves displayed in (E) represent the average density of states extracted from the back-side, Mo-side, and the UHV annealed front-surface [Colour figure can be viewed at wileyonlinelibrary.com]

not deteriorate the absorber much and an in-depth analysis of the back-surface with scanning probe techniques was well justified.

In Figure 3A, the visible grain boundaries of Figure 2A are highlighted together with the *dI*/*dU*-CITS maps at different applied voltages (Figure 3B–D). In all three cases, (U=−1 V, U=0 V, and U=1 V) the maps are relatively featureless, which is in contrast to previously reported top-view measurements on potassium cyanide etched or air exposed CISe absorber layers.[27,28,30] Especially, no distinct grain boundary contrast at $U = 0V$ could be observed, which indicated that the density of states at the grain boundaries was similar to the grain surfaces. The measurements showed some similarity to absorbers after UHV annealing, where a passivation of the defect states at the Fermi-level ($U = 0V$) was observed.[27,29,30] Because the CITS maps at all specific voltages were featureless (no lateral variations), we extracted an average *dI*/*dU* curve from the scanned region, shown in Figure 3A. The curve is shown in Figure 3E as a solid line together with a measurement on the Mo-side (see Figure 2B) and one that was measured after heat induced passivation on the front surface of a CISe absorber synthesized with the same process in the same physical vapor deposition system.[27]

The first thing to note is that the UHV annealed sample and the measurement from the back-surface were very similar. The parts at positive voltages were almost identical whereas the curves at higher negative applied voltages were different. We relate this difference to a different densities of states of the tips, which were certainly different in the two measurements. Important however, was the excellent agreement of the valence band and conduction band onsets. The Fermi-level, which is located at $U = 0V$ was very close to mid-gap, in agreement with the UHV annealed case.[27,29] However, we also note that the valence band and conduction band edges were not sharp and there was substantial tailing into the bandgap region. A possible reason for this will be discussed later in the manuscript.

The measurements on the Mo-side, which mainly consisted of $MoSe_2$ were different and we did see a finite conductance at E_F. Furthermore, the Fermi-level was closer to the conduction band, which points towards n-type doping in agreement with UPS measurements.[14] The finite conductance at E_F was an indication that the Mo-side had a lot of defects and explained why we did not observe a well-defined semiconducting gap as we would expect for $MoSe_2$.

The absence of a clear grain boundary contrast in STS on the back-side is somewhat surprising because it was shown via a combined electron beam induced current (EBIC) and cathodoluminescence (CL) study that carrier collection efficiency and the CL yield were different at distinct grain boundaries. Our STS measurements do not support this interpretation. However, we need to keep in mind that the information depth was very different for EBIC/CL (several hundred nanometers) and STS (<1 nm). Furthermore, the oxygen content may have been very different. In the present study, the cleaving was carried out in a glovebox preventing air exposure. This is usually not done for EBIC/CL measurements, which are much less surface sensitive. Another question to be discussed is the sensitivity limits of the STS measurements to detect changes in work function. This can conveniently be done using the fact that the tunneling conductance can be approximated by the following formula:[40]

$$\frac{dI}{dU} \propto \rho_S(eV)T(d,V,eV) \equiv LDOS(eV). \quad (2)$$

This equation assumes that the density of states of the tip ρ_T is constant for all applied voltages and that the voltage dependence of the tunneling coefficient T is small and can be neglected. The density of states of the sample is denoted with ρ_S. The tunneling coefficient

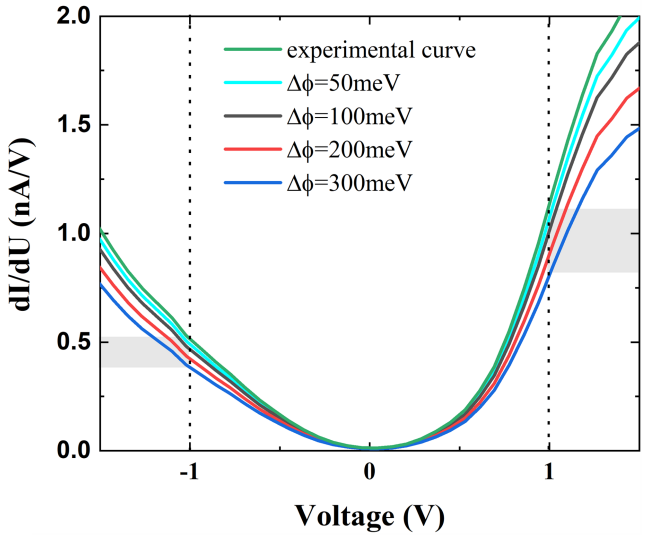

FIGURE 4 Impact of a change in the absorber work function ϕ_S on dI/dU assuming a constant density of states of the sample ρ_S and of the tip ρ_T. A tip sample separation d = 5Å , a sample work function $\phi = 4.5$ eV and a tip radius R=1 nm were assumed for the calculations. The work function difference depicted in the figure is given by $\Delta\phi$=$\phi_{S,A}$-$\phi_{S,B}$. The shaded regions highlight the changes in conductance at a voltage of ±1 V, which corresponds to the voltages shown in Figure 3B,D [Colour figure can be viewed at wileyonlinelibrary.com]

depends on the work function of the tip ϕ_T and the sample ϕ_S, the tip sample separation d and the tip radius R and is given by[40]

$$T(d,\phi_{S,T},V,E) \approx \exp\left[-2(d+R)\frac{2}{3}\sqrt{\frac{2m}{\hbar^2}}\cdot\left(\frac{(\phi_T - E + eV)^{3/2} - (\phi_S - E)^{3/2}}{\phi_T - \phi_S + eV}\right)\right]. \quad (3)$$

Assuming that the density of states of the sample ρ_S is not changing if we change the work function of the sample, we can simulate the effect of a different work function via

$$(dI/dU)_{\phi_{S,B}} = (dI/dU)_{\phi_{S,A}}\frac{T_{\phi_{S,B}}}{T_{\phi_{S,A}}}, \quad (4)$$

where the subscripts A, B denote the regions of different surface work functions at constant density of states of the sample and of the tip.

Figure 4 illustrates how the variations in the work function change the dI/dU curve assuming a constant density of states ρ_S of the sample. In our case, the experimental dI/dU curve was not symmetric, which led to a larger change at positive voltages than at negative ones. Overall, we see that the curve at positive voltages is influenced mostly by the changes in work function. However, it is important to note that we do need a rather large variation in the work function in order to see an effect in the STS spectra. From the graph, we concluded that at least, 100 meV difference is needed to see a clear change in the experimental dI/dU-curves.

4 | KELVIN PROBE FORCE MICROSCOPY MEASUREMENTS

We therefore carried out additional KPFM measurements, which is a technique that is more sensitive to changes in the work function than STS.[33] The results are presented in Figure 5 where a topography image (Figure 5A) and a CPD map (Figure 5B) are depicted. The CPD map is related to the work function via Equation (5).

$$V_{CPD} = \frac{\phi_S - \phi_T}{e}. \quad (5)$$

Consequently, the brighter regions in the CPD map corresponded to regions with higher work functions, assuming a constant work function of the tip. In the topography image, we again observed the grain boundaries as slightly lower regions, in agreement with the STM measurements. Furthermore, we also observed very small dots on the rear-surface. The contact potential difference map showed, in contrast to STS a slightly higher contrast at the grain boundaries. A line profile along such a grain boundary is shown in Figure 5C. The shaded area in the graph highlights the grain boundary region. We did observe a decrease of the topography by approximately 10 nm, together with an increase in the work function of approximately 40 meV. This anti-correlation was observed on all grain boundaries in the image. Comparing this result to the STS measurements (Figure 3) and the calculations (Figure 4) it is clear that values of grain boundary band bending of approximately 40 meV were too small to be detected in STS.

However, one important aspect still needed to be discussed in more detail. A careful inspection of the density of the small dots that cover the complete back-surface showed that, at the grain boundaries the density seemed to be slightly lower (see Figures 2A and 5A). We therefore needed to analyze if the changes of the dot density at the grain boundaries were responsible for the observed work function changes. At least the dots seemed to have an impact on the work function because we also measured variations in CPD on the grain surfaces. The line profiles in Figure 5C showed that the variations were approximately 20–30 mV in the area outside of the shaded region. In Figure 5C, we highlighted all the prominent minima in the topography with green dashed lines whereas the maxima are highlighted with black dotted lines. For both situations (maxima or minima) in the topography, we also measured CPD variations in both directions, that is, no direct correlation between the maxima and minima in topography and CPD. We concluded that the dots are not the main reason for the systematic changes in the work function that we observed at the grain boundaries. However, we realized from this analysis that the dots do have an impact on CPD albeit not always in the same direction.

In the following, we would like to discuss the EDX and XPS results in more detail in order to link them to the SPM measurements.

5 | ELEMENTAL COMPOSITION AT THE REAR-SURFACE

Table 1 summarizes the elemental compositions we measured with EDX and XPS. The EDX measurements were acquired at 20, 15, 7, and 5 kV in order to gain some insights into the compositional changes as a function of depth. In addition to these measurements of the back-side, we also included a measurement carried out at 20 kV on the front-side of the absorber after KCN etching. This measurement can be considered as a reference because an etched stoichiometric CISe absorber layer should exhibit a Cu/In ratio of 1 in the bulk in agreement with our

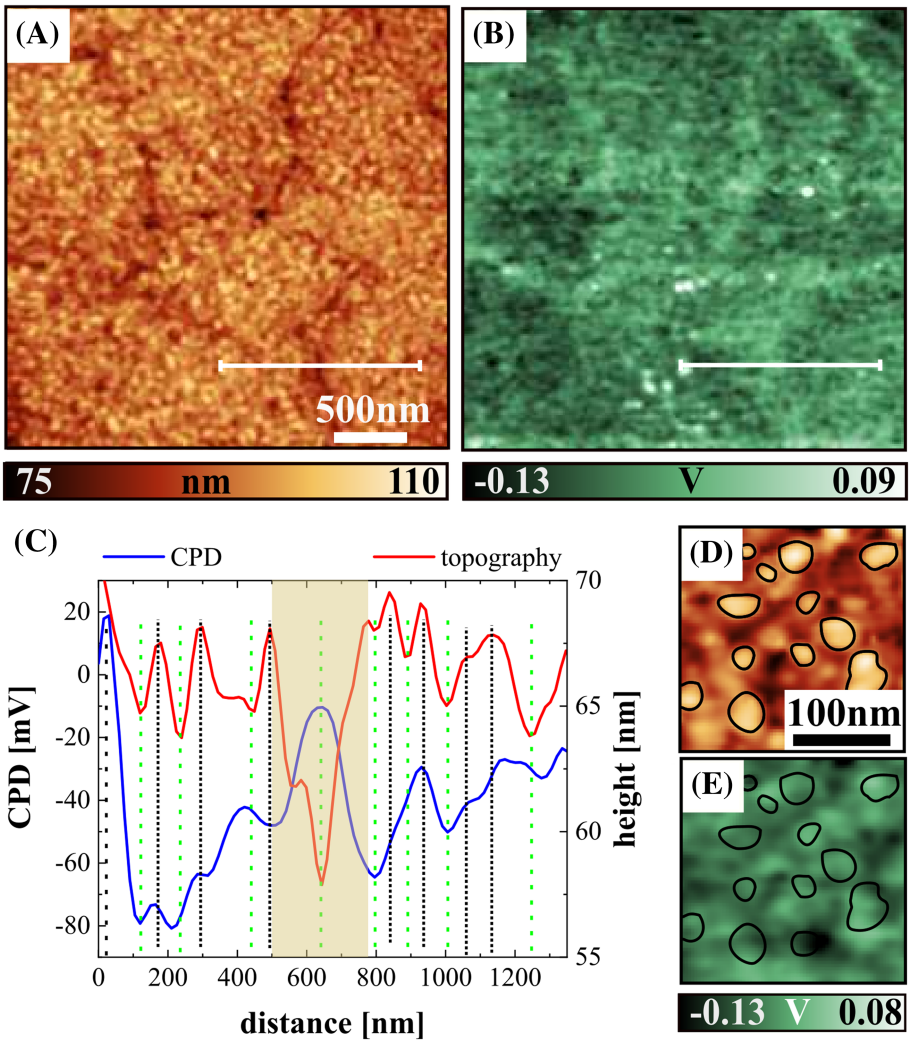

FIGURE 5 KPFM measurements carried out at the back-side of a Cu-rich CISe absorber. (A) surface topography image, (B) surface potential map, (C) line profiles as indicated in (A) and (B). The shaded area highlights the grain boundary region. The green dashed lines indicate local minima in topography whereas the dashed black lines show local maxima in the topography line-scan. (D,E) Topography and CPD map of the small precipitations. Some regions are highlighted in both images to correlate the topographic information to the work function variations [Colour figure can be viewed at wileyonlinelibrary.com]

measurements. The systematic error for the elemental concentration is at least 1 at% for an EDX measurement and consequently the small deviations from the expected values were well within the error of the measurement technique. Although the systematic errors in EDX are large, changes in the composition at varying acceleration voltages are much less susceptible to large errors if the quantification is done with the same characteristic X-ray lines. Consequently, the measurements performed at different acceleration voltages suggested that the Cu-content is slightly higher at the back-contact region. However, EDX measurements are not surface sensitive enough to analyze compositional changes in the near surface region.

XPS measurements are much more surface sensitive (≈ 6–8 nm) than EDX measurements, which are more bulk sensitive (information depth ≈ 0.1–1 μm at 5–20 kV acceleration voltage).[41] Interestingly, the Cu concentration, as deduced via XPS was much higher close the interface with a Cu/In ratio of 1.7. This was a clear indication that excess Cu was present at the back-contact and further strengthens the EDX results. At the Mo-side we measured a small amount of Cu and no In, which corroborated that there was no CISe remainders on the Mo-side. The Mo/(Se+O) ratio is 0.6, which points towards a $MoSe_2$ layer, partially oxidized due to the rather long storage time of this substrate in the glovebox before introduction into the XPS system. The oxygen concentration was more than doubled compared to the back-side absorber, which was introduced directly after the exfoliation. However, residual oxidation of the substrate prior to the growth process cannot be excluded and may also have contributed to the higher oxygen content.

We will now discuss the high resolution scans of the individual elemental transitions acquired via XPS. In Figure 6A, the Cu 2*p* line of the back-side and of the Mo-side are shown. The binding energy of 932.4 eV was in excellent agreement with the reported values for $CuInSe_2$.[42] The Auger parameter, which is only sensitive to the chemical environment and not to changes in binding energy as a result of different band bending, was 1849.7 eV, which was also in good agreement with CISe.[42] The Cu concentration at the Mo-side was only 1 % (see Table 1). In Figure 6D, the Cu 2*p* spectra were normalized to the peak maxima in order to improve the visibility. Within the error of the measurement, we could not observe a significant shift in the binding energy and the Auger lines were too weak to estimate an Auger parameter. The In 3*d* lines are presented in Figure 6B. The binding energy was in accordance with the reported values,[42] and we could not observe Indium at the Mo-side. This showed that the detected Cu that we measured on the Mo side is not bound to CISe. The Se 3*d* lines are depicted in Figure 6C. A clear shift in the binding energy was visible when comparing the two substrates. On the backside the Se $3d_{5/2}$ was located at 54.2 eV whereas on the Mo-side the value

TABLE 1 EDX and XPS compositions

EDX Composition, at%	Cu	In	Se	Cu/In			
Back-side (20 kV)	24 (24)	25 (25)	50 (50)	0.9 (0.9)			
Back-side (15 kV)	28 (28)	24 (24)	48 (48)	1.2 (1.2)			
Back-side (7 kV)	30 (30)	24 (24)	46 (47)	1.3 (1.3)			
Back-side (5 kV)	32 (30)	23 (23)	45 (47)	1.4 (1.3)			
Front-side (20kV)	25	24	51	1.0			
XPS composition [at%]	**Cu2*p***	**In3*d***	**Se3*d***	**Cu/In**	**Na1*s***	**Mo3*d***	**O1*s***
Back-side	29	17	42	1.7	0.5	/	11
Mo-side	1	0	36	/	0.3	38	24

Note. EDX and XPS measurements were acquired on large areas (compared to the grain size) in order to get representative averages. EDX values in brackets were measured after KCN etching of the back side. All samples were etched on the front side prior to the peel off process. All measurements performed on the back side were carried out in one session to limit the error bar. The measurements on the front side were done with another SEM machine and different systematic errors may influence the absolute numbers.

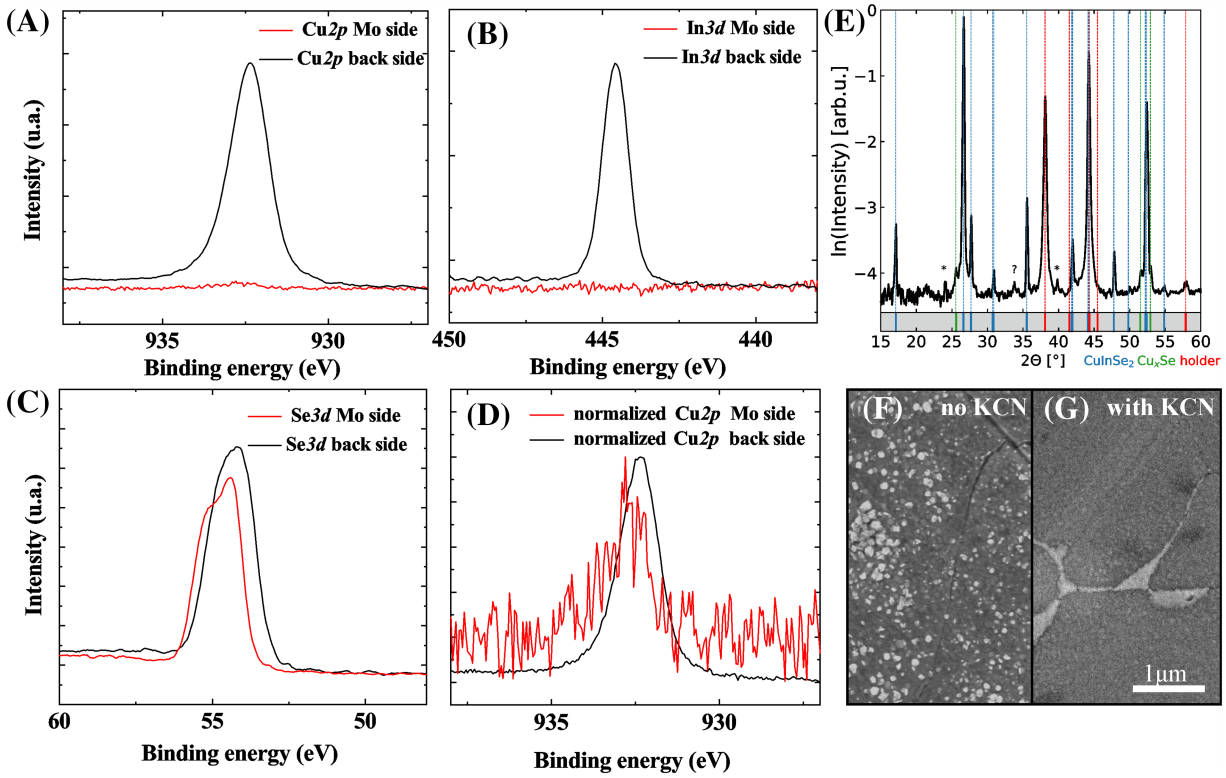

FIGURE 6 (A–D) High-resolution XPS measurements of the back-side and the Mo-side (A) Cu 2*p*, (B) In 3*d*, (C) Se 3*d*, (D) normalized Cu 2*p* curves depicted in (A). (E) Grazing incidence XRD measurement performed on a peeled absorber (the front-side of the absorber was etched whereas the back-side was not). (F) SEM micrograph of the back-side of the absorber prior to KCN etching. (G) Identical absorber after KCN etching. XRD references: $CuInSe_2$:04-007-6152; Cu_xSe: 04-007-6152, ∗: Kβ peak of the (112) and (204) reflex [Colour figure can be viewed at wileyonlinelibrary.com]

was located at 54.4 eV. The shift towards higher binding energies was attributed to a change in the chemical environment of the Selenium from a CISe matrix on the back-side to a $MoSe_2$ matrix on the Mo-side. The measured values of the binding energies were in agreement with reported values.[42,43] The elemental composition of the $MoSe_2$ (Table 1) was not equal to 2 and the large amount of oxygen was likely to influence the $MoSe_2$ concentration we measured. For both surfaces, the Na concentration was on a similar level with approximately 0.5%.

The XPS and the EDX measurements strongly suggested that there was excess Cu at the back contact of the absorber layer. In order to corroborate the existence of a Cu_xSe secondary phase, grazing incidence X-Ray diffraction was used. The results are presented in Figure 6E. It needs to be emphasized that this absorber layer was KCN etched before the peeling process in order to make sure that all the Cu_xSe detected in the diffractogram originated from precipitates in the bulk or from the back contact. We observed a peak at 25.6° and additional shoulders around the (312) CISe peak at 52.39°, which were also reported to originate from Cu_xSe.[19,44] Consequently, the XRD data confirmed that precipitations exist in Cu-rich absorbers, despite the fact that the front surface was etched with KCN prior to the peel off process. In Figure 6F,G, high-resolution SEM measurements are presented, which show the morphology of the CISe back side

prior to KCN etching and after KCN etching. The small white grains completely disappeared after KCN etching, and furthermore, we did observe substantial changes at the grain boundaries. Complementary AFM measurements (not shown) corroborated the observations made with SEM. The grain boundaries measured in AFM however were much deeper compared to the non KCN etched sample. The brighter contrast in SEM as shown in Figure 6G is not indicative of an accumulation of material but rather due to a higher secondary electron yield at the grain boundaries, i.e. a different electron affinity or workfunction. Currently, we assume that the etching rate at the grain boundaries was enhanced, suggesting that there was a larger amount of Cu_xSe present compared to the absorber back-surface. We attribute the small grains in Figure 6F to Cu_xSe precipitates, which were removed during the KCN etching process. EDX measurements performed on the same sample showed a reduction of the Cu/In ratio from 1.4 to 1.3 due to the removal of a Cu_xSe secondary phase.

6 | DISCUSSION AND CONCLUSIONS

The following list summarizes the key findings of the preceding sections.

- The back-side of stoichiometric CISe absorber showed an increased concentration of Cu in the region close to the interface. XRD measurements showed small amounts of a Cu_xSe phase, which could be removed with a subsequent KCN etching of the back-side as evidenced by high resolution SEM micrographs.
- We observed a weak upward band bending of approximately 40 meV at the grain boundaries as measured with KPFM.
- The STS data were similar to the results obtained on UHV annealed CISe absorbers. However, there was still substantial tailing as we did see a gradual decrease of the dI/dU curves into the bandgap region and the absence of sharp conduction and valence bands.
- The Fermi-level was mid-gap, similar to the absorbers surfaces after UHV annealing.[27,29]
- For the Mo-side E_F was closer to the conduction band and we did measure a finite conductance at E_F, which pointed towards a high number of defects in the $MoSe_2$ or very high doping levels.

The most intriguing finding is certainly the high concentration of Cu at the absorber back-side and a non-negligible concentration on the Mo-side. XRD and SEM measurements corroborate that a very thin layer of Cu_xSe formed at the $MoSe_2$/CISe interface due to the Cu-rich growth conditions. This finding is not in accordance with reports on Cu-rich $CuInS_2$ where the back surface did show an Indium enrichment[13] and no indication of a Cu_xSe phase. To the best of our knowledge, there are no reports available where the back-surface of a Cu-rich CISe absorber was investigated with XPS measurements. However there is a lot of literature available for the Cu-poor material. In accordance with TEM measurements[16] of the back-surface, we found a $MoSe_2$ layer which included some Cu. However, no Cu_xSe secondary was observed in their studies. Furthermore, XPS and UPS measurements of the Cu-poor CIGSe/$MoSe_2$ interface also excluded a Cu_xSe secondary phase. They observed an accumulation of Ga and Cu at the rear contact, in accordance with APT measurements.[17]

The present investigation shows that Cu-rich Selenium based absorbers exhibit different surface- and back-surface compositions compared to the absorber bulk. The Cu-rich growth conditions trigger the precipitation of a Cu_xSe secondary phase, which is not present in Cu-poor material and which segregates at both interfaces. In our STM and AFM measurements, we observed that both sides of the rear-interface were covered with very small grains in the order of several tens of nanometers. We did see a correlation of the work function with the grains although we could not observe one distinct value. It rather seemed like randomly oriented small grains that exhibit slightly different work functions. We assign the small grains and their variations in work function on the grain surfaces (≈20 meV) to Cu_xSe. This conclusion was drawn on the basis of our XPS and EDX measurements, which showed a clear increase in Cu at the back-side of the CISe absorbers and the XRD measurements showed that residual Cu_xSe was present in the absorber layer. From XRD, we cannot rule out that there was no Cu_xSe present in the bulk of the absorber. However, the EDX and SEM measurements confirm that at least a part of the Cu_xSe was present at the rear-side.

The work function changes at the grain boundaries that we measured in this study are inverted compared to results reported by Marron et al.[20] However, these investigations were performed on Cu-poor $CuGaSe_2$. It is currently not clear if the differences can be assigned to a different Cu concentration at the grain boundaries, which favors upward band bending for the case of Cu-rich material and downward band bending for Cu-poor material. More investigations on Cu-poor material with SPM techniques are mandatory to unambiguously prove this hypothesis. KCN etching of the back-side showed an increased etching rate at the grain boundaries compared to the surface. We attribute this to a larger amount of Cu_xSe at the grain boundaries.

Another important point that needs to be discussed further are the STS results. Based on our XPS findings, the back-surface of the CISe were partially covered with Cu_xSe. In the present study, we focused on large area scans where the dI/dU maps averaged over large areas covered with a large number of small grains. This fact may explain the rather undefined band edges that we observed in our measurements. High resolution STS measurements are necessary to disentangle the signal from the small grains from the one of the underlying substrate. At present this was not possible due to the duration of the CITS scans (approximately 15 hours), which imposed very strict limits for the maximum allowed temperature drift during STS measurements.

We finally would like to discuss the implications for devices. Our measurements corroborate that Cu_xSe precipitations do not only form at the front contact but also at the rear-surface under Cu-rich growth conditions in CISe. The interface recombination velocities are likely to be higher than for a pure $MoSe_2$/CISe interface since the $MoSe_2$ is a layered material with pure van der Waals bonding along the growth direction, that is, no dangling bonds. It is likely that the Cu_xSe secondary phase makes the interface worse and thereby reduces the PCE of the final device. Furthermore, band bending is different than in Cu-poor $CuGaSe_2$. Although at present we cannot disentangle the influence of the Ga/In from the different Cu content, the results still showed the composition has important consequences for the properties of the grain boundaries as also described in a recent APT study for $CuInS_2$.[45]

The reported measurements showed an increased concentration of Cu at the grain boundaries in Cu-rich $CuInS_2$. If we assume a similar grain boundary chemistry in Cu-rich CISe, excess Cu would segregate out at all interfaces (front, back, and grain boundaries) with distinct opto-electronic properties compared to the Cu-poor absorbers. The SEM measurements performed before and after KCN etching of the back side are in line with these observations since we do see a preferential etching of the grain boundaries.

In summary, we showed that for stoichiometric CISe absorbers the rear-surface exhibited an accumulation of Cu, which we assigned to a Cu_xSe secondary phase. This is in contrast to Cu-poor CIGSe where a Cu and Ga enrichment were measured. We measured a slight upward band bending of approximately 40 meV at the grain boundaries and showed that such low values cannot be measured with STS. The density of states of the rear-surface was similar to that of the UHV annealed absorbers. Similar measurements on Cu-poor material need to be carried out. Our finding must be taken into account when discussing why Cu-rich material does not perform well in solar cells compared to Cu-poor absorbers. The detrimental Cu_xSe secondary phase, which can be etched off on the front-side is also present at the rear-surface, increasing the back-surface recombination velocity. In the absence of a suitable back-surface field, this may be very detrimental for device performance. Finally, we would like to note that it is likely that similar processes occur in other Selenium based absorbers layers such a $Cu_2ZnSnSe_4$ where Cu-poor growth conditions are also mandatory to reach the current record power conversion efficiencies.

ACKNOWLEDGEMENTS

The authors acknowledge funding from the Fonds National de la Recherche Luxembourg (FNR), project "Sunspot", Nr. 11244141. A.E. and H.M. acknowledge the Deutsche Forschungsgemeinschaft through project MO 2345/5-1 for funding. The authors thank Susanne Siebentritt, Florian Ehre, and Phillip Dale for sample supply and useful discussions. Michele Melchiorre is acknowledged for SEM and EDX measurements. Furthermore, the authors like to thank Thomas Schuler, Ulrich Siegel, Bernd Uder, and Nicolas Tournier for technical assistance.

ORCID

Alex Redinger https://orcid.org/0000-0002-2958-3102

REFERENCES

1. Nakamura M, Yamaguchi K, Kimoto Y, Yasaki Y, Kato T, Sugimoto H. Cd-Free Cu (In,Ga)(Se,S)$_2$ Thin-film solar cell with record efficiency of 23.35 %. *IEEE J Photovoltaics*. 2019;6(6):1863-1867.
2. Powalla M, Paetel S, Hariskos D, et al. Advances in cost-efficient thin-film photovoltaics based on Cu(In,Ga)Se2. *Engineering*. 2017;3(4):445-451.
3. Carron R, Nishiwaki S, Feurer T, et al. Advanced alkali treatments for high-efficiency Cu(In,Ga)Se_2 solar cells on flexible substrates. *Adv Energy Mater*. 2019;9(24):1900408.
4. Dullweber T, Lundberg O, Malmström J, et al. Back surface band gap gradings in Cu(In,Ga)Se_2 solar cells. *Thin Solid Films*. 2001;387(1-2):11.
5. Gloeckler M, Sites JR. Band-gap grading in Cu(In,Ga)Se_2 solar cells. *J Phys Chem Solids*. 2005;66(11):1891.
6. Kavalakkatt J, Abou-Ras D, Haarstrich J, et al. Electron-beam-induced current at absorber back surfaces of Cu(In,Ga)Se_2 thin-film solar cells. *J Appl Phys*. 2014;115(1):014504.
7. Vermang B, Wätjen JT, Fjällström V, et al. Highly reflective rear surface passivation design for ultra-thin Cu(In,Ga)Se_2 solar cells. *Thin Solid Films*. 2015;582:300.
8. AbuShama J, Noufi R, Johnston S, Ward S, Xu X. Improved performance in $CuInSe_2$ and surface-modified $CuGaSe_2$ solar cells. *Conference Record of the Thirty-first IEEE Photovoltaic Specialists Conference*. 2005:299–302. https://doi.org/10.1109/PVSC.2005.1488128
9. Valdes NH, Lee J, Shafarman WN. Ag alloying and KF treatment effects on low bandgap $CuInSe_2$ solar cells. *IEEE J Photovoltaics*. 2019;9(3):906.
10. Feurer T, Bissig B, Weiss TP, et al. Single-graded CIGS with narrow bandgap for tandem solar cells. *Sci Technol Adv Mater*. 2018;19(1):263.
11. Elanzeery H, Babbe F, Melchiorre M, Werner F, Siebentritt S. High-performance low bandgap thin film solar cells for tandem applications. *Prog Photovolt Res Appl*. 2018;26(7):437.
12. Feurer T, Carron R, Torres Sevilla G, et al. Efficiency improvement of near-stoichiometric $CuInSe_2$ solar cells for application in tandem devices. *Adv Energy Mater*. 2019;9(35):1901428.
13. Scheer R, Lewerenz HJ. Formation of secondary phases in evaporated $CuInS_2$ thin films: a surface analytical study. *J Vac Sci Technol A Vacuum, Surf, Films*. 1995;13:1924.
14. Bär M, Nishiwaki S, Weinhardt L, Pookpanratana S, Shafarman WN, Heske C. Electronic level alignment at the deeply buried absorber/Mo interface in chalcopyrite-based thin film solar cells. *Appl Phys Lett*. 2008;93(4):042110.
15. Bär M, Weinhardt L, Heske C, Nishiwaki S, Shafarman WN. Chemical structures of the Cu (In,Ga)Se_2/Mo and Cu(In,Ga)$(S,Se)_2$/Mo interfaces. *Phys Rev B: Condens Matter Mater Phys*. 2008;78(7):075404.
16. Wada T, Kohara N, Nishiwaki S, Negami T. Characterization of the Cu(In,Ga)Se_2/Mo interface in CIGS solar cells. *Thin Solid Films*. 2001;387(1-2):118.
17. Keller J, Schlesiger R, Riedel I, et al. Grain boundary investigations on sulfurized Cu(In,Ga)$(S,Se)_2$ solar cells using atom probe tomography. *Sol Energy Mater Sol Cells*. 2013;117:592.
18. Nadenau V, Hariskos D, Schock HW, et al. Microstructural study of the CdS/CuGaSe2 interfacial region in $CuGaSe_2$ thin film solar cells. *J Appl Physiol*. 1999;85(1):534-542.
19. Alberts V, Swanepoel R, Witcomb MJ. Material properties of CuInSe2 prepared by H2Se treatment of CuIn alloys. *J Mater Sci*. 1998;33(11):2919-2925.
20. Marrón DF, Meeder A, Sadewasser S, et al. Lift-off process and rear-side characterization of $CuGaSe_2$ chalcopyrite thin films and solar cells. *J Appl Phys*. 2005;97(9):094915.
21. Siebentritt S, Gütay L, Regesch D, Aida Y, Deprédurand V. Why do we make Cu(In,Ga)Se_2 solar cells non-stoichiometric? *Sol Energy Mater Sol Cells*. 2013;119:18.
22. Babbe F, Choubrac L, Siebentritt S. Quasi Fermi level splitting of Cu-rich and Cu-poor Cu(In,Ga)Se_2 absorber layers. *Appl Phys Lett*. 2016;109(8):082105.
23. Regesch D, Gütay L, Larsen JK, et al. Degradation and passivation of $CuInSe_2$. *Appl Phys Lett*. 2012;101(11):112108.
24. Spindler C, Babbe F, Wolter MH, et al. Electronic defects in Cu(In,Ga)Se_2: Towards a comprehensive model. *Phys Rev Mater*. 2019;3(9):090302.
25. Lokhande CD, Hodes G. Preparation of $CuInSe_2$ and $CuInS_2$ films by reactive annealing in H_2Se OR H_2S. *Sol Cells*. 1987;21(1-4):215.

26. Elanzeery H, Melchiorre M, Sood M, et al. Physical review materials 3 , 055403 (2019) challenge in Cu-rich $CuInSe_2$ thin film solar cells : defect caused by etching. *Phys Rev Mater*. 2019;3(5):55403. https://doi.org/10.1103/PhysRevMaterials.3.055403
27. Boumenou CK, Babbe F, Elizabeth A, et al. Passivation of the $CuInSe_2$ surface via cadmium pre-electrolyte treatment. *Phys Rev Mater*. 2020;4:045405.
28. Mönig H, Smith Y, Caballero R, et al. Direct evidence for a reduced density of deep level defects at grain boundaries of $Cu(In,Ga)Se_2$ thin films. *Phys Rev Lett*. 2010;105(11):116802.
29. Mönig H, Lockhorn D, Aghdassi N, et al. Heat induced passivation of $CuInSe_2$ surfaces: a strategy to optimize the efficiency of chalcopyrite thin film solar cells?. *Adv Mater Interf*. 2014;1(2):1300040.
30. Bröker S, Kück D, Timmer A, et al. Correlating the local defect-level density with the macroscopic composition and energetics of chalcopyrite thin-film surfaces. *ACS Appl Mater Interf*. 2015;7(23):13062.
31. Chen CJ. *Introduction to Scanning Tunneling Microscopy*: Oxford University Press; 2007.
32. Sadewasser S, Glatzel T. *Kelvin Probe Force Microscopy*: Springer Series in Surface Science; 2012.
33. Zerweck U, Loppacher C, Otto T, Grafström S, Eng LM. Accuracy and resolution limits of Kelvin probe force microscopy. *Phys Rev B Condens Matter Mater Phys*. 2005;71(12):125424.
34. Deprédurand V, Bertram T, Siebentritt S. Influence of the Se environment on Cu-rich CIS devices. *Phys B Condens Matter*. 2014;439:101-104.
35. Goldstein J, Newbury DE, Joy DC, et al. *Scanning electron microscopy and X-ray microanalysis*. Berlin Heidelberg: Springer-Verlag; 2003.
36. Ross RT. Some thermodynamics of photochemical systems. *J Chem Phys*. 1967;46(12):4590.
37. Shockley W, Queisser HJ. Detailed balance limit of efficiency of p-n junction solar cells. *J Appl Phys*. 1961;32(3):510.
38. Rühle S. Tabulated values of the Shockley-Queisser limit for single junction solar cells. *Sol Energy*. 2016;695:139-147.
39. Kirchartz T, Márquez JA, Stolterfoht M, Unold T. Photoluminescence-based characterization of Halide perovskites for Photovoltaics. *Adv Energy Mater*. 2020:1904134.
40. Wagner C, Franke R, Fritz T. Evaluation of I (V) curves in scanning tunneling spectroscopy of organic nanolayers. *Phys Rev B Condens Matter Mater Phys*. 2007;75:235432.
41. Abou-Ras D, Kirchartz T, Rau U. *Advanced Characterization Techniques for Thin Film Solar Cells*: Wiley-VCH; 2016.
42. NIST X-ray Photoelectron Spectroscopy Database. *NIST Standard Reference Database Number 20*, Vol. 20899. Gaithersburg MD: National Institute of Standards and Technology; 2000. https://doi.org/10.18434/T4T88K
43. Zhao Y, Lee H, Choi W, Fei W, Lee CJ. Large-area synthesis of monolayer $MoSe_2$ films on SiO_2/Si substrates by atmospheric pressure chemical vapor deposition. *RSC Adv*. 2017;7(45):27969.
44. Robert EVC, de Wild J, Dale PJ. Reaction chemistry of group IV containing copper chalcogenide semiconductors Cu_2MX_3(M = Sn, Ge and X = S, Se). *J Alloys Compd*. 2017;130:1307-1316.
45. Schwarz T, Lomuscio A, Siebentritt S, Gault B. On the chemistry of grain boundaries in $CuInS_2$ films. *Nano Energy*. 2020:105081.

How to cite this article: Kameni Boumenou C, Elizabeth A, Babbe F, Debot A, Mönig H, Redinger A. Electronic and compositional properties of the rear-side of stoichiometric $CuInSe_2$ absorbers. *Prog Photovolt Res Appl*. 2020;1–11. https://doi.org/10.1002/pip.3380